



The Wagging Plasma Tail of Comet C/2020 S3 (Erasmus)

Jing Li , Yoonyoung Kim , and David Jewitt

Department of Earth, Planetary and Space Sciences, University of California, Los Angeles, CA 90095, USA; jingli@epss.ucla.edu

Received 2022 July 31; revised 2023 October 12; accepted 2023 October 23; published 2023 November 29

Abstract

Long-period comet C/2020 S3 (Erasmus) reached perihelion at 0.398 au on UT 2020 December 12.67, making it a bright, near-Sun object. Images taken between 2020 mid-November and December using the HI-1 camera and COR2 coronagraph on board STEREO-A, as well as the LASCO/C3 coronagraph on board SoHO, show significant variations in the plasma tail position angles. To analyze these variations, a simple technique was developed to calculate the aberration angles. These angles are defined as the angle between the Sun–comet line and the tail axis, measured in the orbital plane. The aberration angles were found to range from $1^{\circ}2$ to $46^{\circ}8$, with an average (median) value of approximately $20^{\circ}3$ ($16^{\circ}3$). By considering the aberration angles, the solar wind radial velocities during the observations were inferred to range from 73.9 to 573.5 km s^{-1} , with a mean (median) value of approximately 205.5 km s^{-1} (182.3 km s^{-1}). Throughout the observations, two periods were identified where the tails showed forward tilting, which cannot be explained by aberration alone. In one case, this anomalous position angle was sustained for at least 11 days and is possibly due to corotating interaction regions. In the other case, the tail exhibited dramatic excursions from 180° to 150° back to 210° over a limited period of around 34 hr. This behavior is tentatively explained as a consequence of the interaction with a halo coronal mass ejection that was launched from NOAA Active Region 12786 and arrived at comet C/2020 S3 during the time when the tail displayed its wagging behavior.

Unified Astronomy Thesaurus concepts: Comet tails (274); Solar wind (1534)

Supporting material: animations

1. Introduction

Long-period comet C/2020 S3 (Erasmus; hereafter “S3”) was discovered on UT 2020 September 17 by the Asteroid Terrestrial-impact Last Alert System (ATLAS) sky survey.¹ It has osculating semimajor axis $a = 194.9$ au, eccentricity $e = 0.998$, and inclination $i = 19^{\circ}9$. (The barycentric elements are very similar at $a = 190$ au, $e = 0.998$, and $i = 19^{\circ}9$). As such, S3 has a likely origin in the Oort cloud but it is not a dynamically new object (for which $a > 10^4$ au is required). S3 reached its perihelion on UT 2020 December 12.67 at 0.398 au. The perihelion water production rate was $Q_{\text{H}_2\text{O}} = 4 \times 10^{29}$ s^{-1} (Combi et al. 2023), corresponding to a mass production rate in gas $\sim 12,000$ kg s^{-1} . As the comet approached its perihelion, the solar elongation as seen from Earth decreased from 46° (mid-November) down to 10° (mid-December) rendering ground-based observations increasingly difficult. However, the comet was captured by the Sun-observing Solar Terrestrial Relations Observatory-A (STEREO-A) and Solar and Heliospheric Observatory (SoHO) spacecraft both before and after its perihelion, providing the data set we analyze here.

As is well known from the study of other comets, dust and gas move differently once released from the nucleus. Cometary dust is expelled from the sublimating nucleus by gas drag, typically attaining a size-dependent terminal speed that is small compared to the thermal speed V_{th} of gas molecules. Once ejected, the motion of dust is controlled by solar gravity and

radiation pressure. The force due to solar wind drag is at least an order of magnitude smaller than radiation pressure, and can be ignored (Ragot & Kahler 2003). Comet dust tails are usefully represented by syndynes marking the loci of positions of particles of a given size released continuously from the comet and synchrones which show the loci of positions of particles having a range of sizes but released at a common time (Finson & Probstein 1968).

Different forces influence the ion tails. Gas molecules become ionized primarily by solar UV photons and are swept up by the passing solar wind to form the comet’s plasma tail, as first explained by Biermann (1951). In brief, gas molecules leave the comet nucleus with a speed comparable to the thermal speed appropriate to the temperature of the sublimating surface, typically $V_{\text{th}} \sim 1$ km s^{-1} at 1 au, while the orbital motion of the comet is more comparable to the Kepler speed, $v_K \sim$ a few tens of kilometers per second at 1 au. Both speeds are small compared to that of the solar wind, which sweeps past the comet at a range ~ 200 to ~ 750 km s^{-1} (Hundhausen 1968), and expands outward from the Sun in a roughly radial direction. In interplanetary space, the plasma pressure carried by the solar wind is bigger than the magnetic field pressure so that the magnetic fields from the Sun are frozen in and carried by the solar wind. As a result, cometary ions are picked up by interplanetary magnetic fields via the Lorentz force and form a plasma tail that is characteristically aligned usually close to the Sun–comet line.

For these reasons, the dust and plasma tails are typically spatially separated and appear distinct in the plane of the sky. Whereas the plasma tails are straight and nearly radial to the Sun, dust tails are commonly diffuse and curved in the plane of the sky as a result of the combined radiation pressure and orbital motion. The directions of both types of tail should

¹ <https://minorplanetcenter.net/mpec/K20/K20SB9.html>

Table 1
Instrument Parameters

Instrument	Field of View	Pixel Size	Bandpass (nm)
HI-1/STEREO-A	4°–24° (15–90 R_{\odot}) ^a	71''/9	630–730
COR2/STEREO-A	0°5–3°8 (2–15 R_{\odot}) ^b	14''/7	650–750
C3/SoHO	1°–8° (3.7–30 R_{\odot}) ^b	56''/0	400–835 ^c

Notes.

^a The wide-field camera is aimed at an angle 14° off the solar limb from the principal axis of the instrument.

^b Both instruments are coronagraphs. The angles quoted are the inner and outer edges of the field of view, measured from the Sun’s center.

^c The filter wheel contains blue (420–520 nm), orange (540–640 nm), deep red (730–835 nm), infrared (860–1050 nm), and broadband clear (400–850 nm) filters. A narrowband H α (2 nm) filter is mounted in a wheel holding three polarizers. However, the clear filter is normally used for the observations, which is the case for the current study.

change smoothly in response to the changing observer–Sun–comet geometry. A third, very narrow and typically faint type of tail has been associated with resonance fluorescence from neutral sodium atoms (Cremonese et al. 2002). Sodium atoms have a very large solar radiation pressure acceleration (e.g., $>100 \times$ solar gravity), and so closely track the antisolar direction. For example, a sodium tail was recently reported on asteroid 3200 Phaethon near perihelion using the same instruments as we use in this work (Hui 2023; Zhang et al. 2023). However, our data provide no clear evidence for a neutral sodium tail perhaps for the reason that S3 is not as bright as comet C/1995 O1 Hale–Bopp (Cremonese et al. 1997).

Although plasma tails are roughly aligned with Sun–comet lines, they often show dynamic fine structures imprinted by the local solar wind environment. In fact, the existence of the solar wind was first realized from the appearance of cometary plasma tails (Biermann 1951; Alfvén 1957; Parker 1958; Brandt 1968). It is frequently observed that plasma tails appear cutoff in so-called disconnection events (DEs; Niedner & Brandt 1978; Oyama & Hirao 1985; Wegmann 2000; Voelzke 2005). Suggested causes of DEs include variable ion production rates in the cometary gas (Ip & Mendis 1976), interplanetary shock waves, the comet passing through a heliospheric current sheet (i.e., a sector boundary; Niedner & Brandt 1979), and the impact of coronal mass ejections (CMEs; Vourlidis et al. 2007; Jia et al. 2009). For their visibly disturbed plasma tails, sungrazing comets are studied as probes to infer solar coronal physical conditions (Uzzo et al. 2001; Bryans & Pesnell 2012; Downs et al. 2013; Jones et al. 2018; Cheng et al. 2020; Nisticò et al. 2022). These comets also provide good opportunities to study the constituents of the cometary coma and plasma tails, for example, with the UltraViolet Coronagraph Spectrometer (UVCS; Kohl et al. 1995) on board the SoHO satellite (Povich et al. 2003; Raymond et al. 2018, 2022). These observations show that of the cometary emission lines, HI Ly α is the strongest UV emission line in the cometary coma due to sunlight scattered by H atoms produced from H₂O photo-dissociation. An ion tail consisting of C III has also been observed by UVCS as covered in the works by Povich et al. (2003) and Raymond et al. (2018, 2022).

Because plasma tail appearances reflect the local solar wind environment, a direct application of comet plasma tails is to infer the solar wind radial velocity using the sky plane position

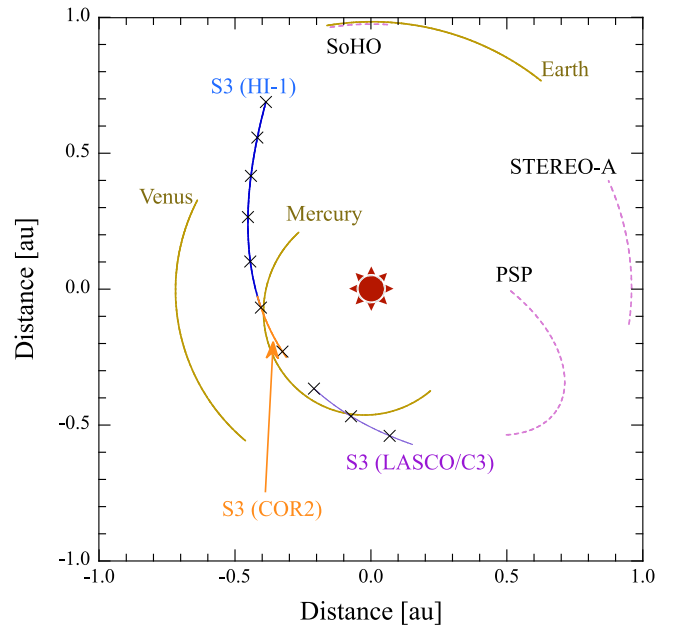


Figure 1. Plan view of the orbital paths of S3, the planets, STEREO-A, SoHO, and PSP in heliocentric Cartesian coordinates during the observing period, from 2020 mid-November to end-December. All objects orbit counter-clockwise. The comet trajectories are plotted as blue, orange and purple arcs corresponding to observations made with the HI-1, COR2 and LASCO/C3 cameras, respectively. Tick marks “X” are plotted every 5 days on the S3 path starting with DOY 318. Three terrestrial planets are represented by brown. The spacecraft are plotted with dashed pink curves.

angles of the tails. Because of the comet’s motion, the tail forms an angle with respect to the Sun–comet line, defining the so-called aberration angle, ε . In the comet orbital plane, the angle is simply written as follows (Alfvén 1957) in the presence of solar wind

$$\varepsilon = \tan^{-1} \left(\frac{v_t}{w_r - v_r} \right), \quad (1)$$

where v_t and v_r represent the perpendicular and radial components of the comet orbital velocities, respectively, w_r represents the solar wind radial velocity. Past measurements of 60 comets yield typical aberration angles $\varepsilon \sim 5^\circ$ (Belton & Brandt 1966; Brandt 1968). However, recent measurements show that ε can span a wider range, $5^\circ \lesssim \varepsilon \lesssim 30^\circ$ (Cheng et al. 2020).

The aberration angle can be obtained from the comet tail in various ways based on the fact that the plasma tail orientation is dictated by the comet’s orbital motion and the solar wind. One way is to fit to the tail position angles by assuming the solar wind velocity at the location of the comets. This is achieved by a coordinate transfer from the orbital plane to the observer’s projected sky plane (Belton & Brandt 1966; Niedner et al. 1978). Several comets have been observed by the Solar Mass Ejection Imager (SMEI) on the Coriolis spacecraft, which follows a polar orbit above the Earth’s terminator. The combined fish-eye sky map shows the entire sky, revealing comet tails as long as 0.5 au. The aberration angles along with solar wind speeds are obtained at multiple locations along the tail in a coordinate system originating at the comets (Buffington et al. 2008; Clover et al. 2010;

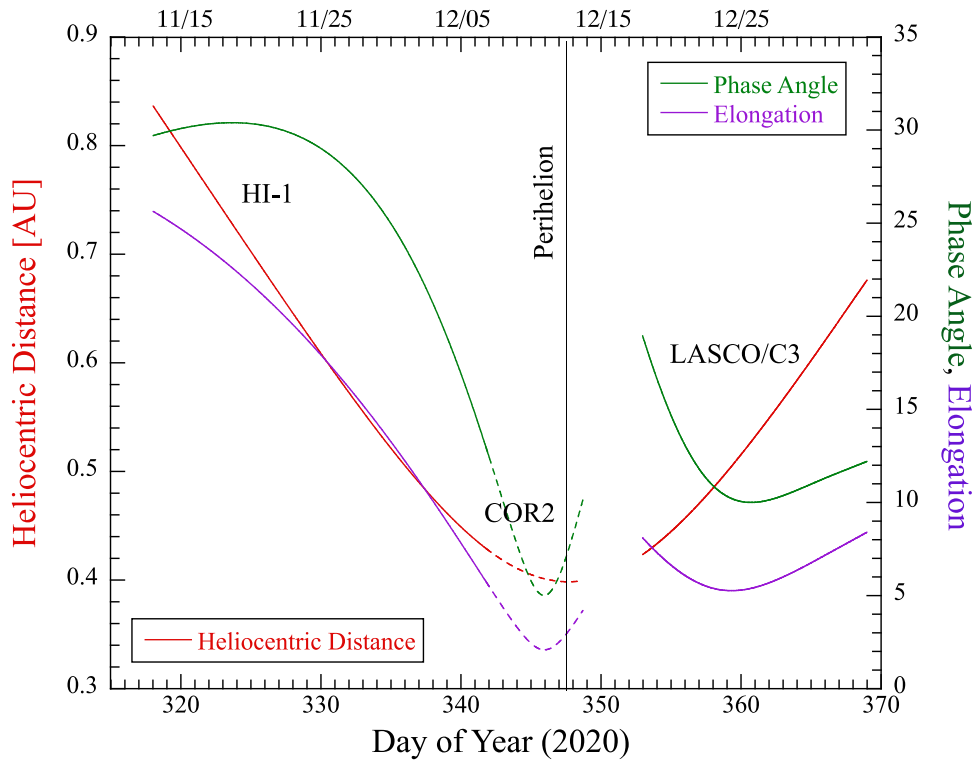


Figure 2. Observational geometry as a function of time. The S3 observations are made with the HI-1 wide-field camera (solid lines) and COR2 coronagraph (dotted lines) on STEREO-A. After DOY 350, S3 is detected by the LASCO/C3 coronagraph on SoHO (solid lines). Perihelion is at UT 2020 December 12.67, indicated by the gray vertical line. Heliocentric distance, phase angle, and elongation are represented by red, green, and purple, respectively. Calendar dates are indicated along the top axis.

Jackson et al. 2013). Using the STEREO twin spacecraft, Cheng et al. (2020) reconstruct comet images in three-dimensional space, and obtain the comet aberration angles and solar wind velocities. They adapted their method to use single telescope measurements to determine the aberration angles (Cheng et al. 2022). A different technique using time-series images of the comet is employed by Ramanjooloo & Jones (2022) to infer the solar wind radial velocity from the comet aberration angles. In this paper, we report near-Sun observations of S3, focusing on the plasma tail. We estimate the comet aberration angles and solar wind speeds from the position angles and the known geometry of observation. We also introduce a new method to determine the aberration angles.

The paper is organized as follows: in Section 2, the STEREO-A and SoHO data are described. In Section 3, measurements of the comet tails are described and analyzed. The results are discussed in Section 4 and a summary is given in Section 5.

2. Observations

S3 was observed using two spacecraft: STEREO-A (Kaiser et al. 2008), and SoHO (Domingo et al. 1995). In chronological order, the comet was first recorded by a wide-field camera (HI-1), then by a narrow-field coronagraph (COR2), both on board STEREO-A (Howard et al. 2008; Eyles et al. 2009), then by a coronagraph (C3) which is a part of the Large Angle and Spectrometric Coronagraph Experiment (LASCO; Brueckner et al. 1995) on board SoHO. The observational times and instrument parameters are listed in Table 1. The two STEREO-

A cameras have similar spectral coverage with filter bandwidths from 630 to 730 nm for HI-1 and from 650 to 750 nm for COR2, but they have different fields of view and angular resolutions. The LASCO/C3 camera has a filter wheel containing five filters: a wide bandpass filter (400–835 nm), blue, orange, deep red, and infrared filters. The clear filter is normally used for observations, which is the case for the current study.

The comet observations lasted from 2020 mid-November to 2021 January. STEREO-A is a Sun-orbiting spacecraft drifting away from Earth, but along the Earth's orbit. SoHO orbits the Earth-Sun L1 Lagrangian points; as a result, the observing geometry at any time differs between the two. For easy reference, Figure 1 shows a plan view of the orbital path of S3, together with the terrestrial planets and the STEREO-A, SoHO and, for reference, the Parker Solar Probe (PSP) spacecraft during the observing period. Figure 2 shows the temporal variation of the geometric parameters as S3 crossed the HI-1 (solid curves), COR2 (dotted curves), and C3 (solid curves at later time) cameras. S3 exited the COR2 field of view almost exactly 1 day after perihelion.

The comet stayed in the wide-angle HI-1 camera field for 24 days from UT 2020 November 13.0 to December 7.0. It then crossed the narrower field of view of COR2 from UT December 6.5 to 13.7. Starting about 4.3 days later, it was observed by LASCO/C3, from 2021 December 18.0 to January 3.0. The comet image quality becomes too poor to obtain reliable measurements of the tail position angles after 2021 January 1. Therefore, we use only the combined observational data between 2020 mid-November and the end of December. S3 was not observed at the same time from

different vantage points and, therefore, a stereoscopic view like that obtained by Cheng et al. (2020) with the twin STEREO spacecraft is not available for this work.

We downloaded level-0 data from the STEREO-A site² and further processed them to level 1 using the standard IDL procedure, *secchi_prep*, in the SolarSoftWare (SSW) package (Freeland & Handy 1998). This step included flat-field and stray light corrections. We applied a data reduction technique similar to that described in Jewitt & Li (2010), with the purpose being to obtain “clean” images free of stars and transient features such as CMEs. This was achieved by subtracting a rolling median image of the corona from individual images within the sequence. The comet was located in the STEREO-A images using the World Coordinate System (WCS) provided in the STEREO-A FITS headers (Thompson & Wei 2010) combined with JPL Horizons comet ephemerides in celestial coordinates. Examples of final processed images from HI-1 and COR2 cameras are shown in Figure 3 in the top and middle panels, respectively.

We downloaded the C3/LASCO data from the LASCO level_0.5 data site.³ To remove background coronal emission, a minimal image was obtained by adopting the minimum values at each pixel from all images. The final images were obtained by subtracting the minimal image from the original C3 images. While the spacecraft attitude data are absent in the C3 FITS headers (Bill Thompson, private communication), the comet was bright enough to be tracked by a computer algorithm from image to image. An example of a processed image from C3 is shown in Figure 3 in the bottom panel.

In Figure 3, projected comet paths are overlaid on each image from the three different instruments for their respective observation periods. The comet moves from right to left in all three instrument’s field of view.

3. Comet Tails

To enhance the signal-to-noise levels, we computed image medians using data taken over time spans between 0.2 and 1.0 days (Tables 2, 3, and 4). All three tables list the dates and times of the image medians, position angles of anti-Sun (θ_{-s}), and anti-orbital-motion (θ_{-v}) directions of the measured position angles of the dust (θ_{dust}) and plasma (θ_{plasma}) tails. Although dust is not our primary interest, we computed syndyne and synchrone dust models to compare with the data, assuming a range of particle sizes and ejection dates. In these models, dust particles are released at zero velocity and accelerated by the gravity of the Sun and by radiation pressure. The particle size is described by a dimensionless parameter, β , equal to the ratio of the acceleration induced by radiation pressure to that owing to local solar gravity (Bohren & Huffman 1983). To a first approximation, $\beta \sim a^{-1}$, where a is the particle radius in microns. These models not only reveal an estimate of the effective particle sizes in the dust tail, they also serve the purpose of identifying and separating dust from plasma tails in the plane of the sky. The synchrone and syndyne curves are superimposed on the comet image in Figures 4, 5, and 6. Synchrone were computed for ejection times of 20, 40, 60, 80, and 100 days prior to the date of observation (curves from bottom to top, in the figures). Synchrone were computed for

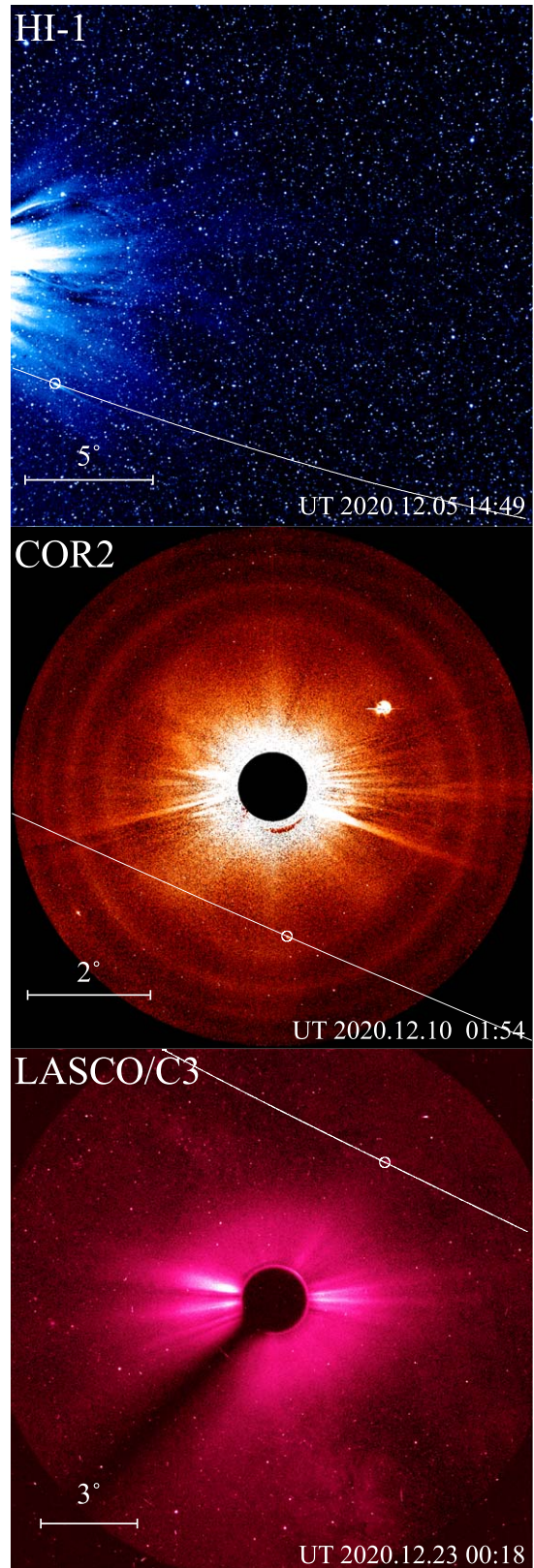


Figure 3. Full coronal images from the wide-field camera HI-1 (top), the narrow-field camera COR2 (middle) both on STEREO-A, and the LASCO/C3 coronagraph (bottom) on SoHO. The projected comet paths are plotted with solid white curves. The comet positions at the times of images are circled on each image.

$\beta = 1, 0.3, 0.1, 0.03,$ and 0.01 (curves from bottom to top), corresponding to nominal particle radii of 1, 3, 10, 30, and 100 μm , respectively.

² https://stereo-ssc.nascom.nasa.gov/data/ins_data/secchi/L0/a/img/

³ https://umbra.nascom.nasa.gov/pub/lasco_level05/960430/c3/

Table 2
Measurements From HI-1

Date	Days ¹	θ_{-S} ²	θ_{-V} ³	θ_{dust} ⁴	θ_{plasma} ⁵	ϵ ⁶	w_r ⁷	w_{nonr} ⁸
2020-11-13 14:29	1.0	268.3	281.6	...	268.2 ± 1.7	−8.2	...	−63.5
2020-11-14 19:15	1.0	268.4	281.6	...	268.7 ± 3.0
2020-11-16 00:14	1.0	268.4	281.5	...	268.0 ± 1.3	−7.1	...	−61.0
2020-11-17 05:00	1.0	268.3	281.4	...	267.0 ± 3.3	−13.4	...	−86.8
2020-11-18 09:45	1.0	268.3	281.3	...	267.1 ± 1.2	−11.0	...	−78.4
2020-11-19 14:29	1.0	268.1	281.2	...	267.2 ± 2.6	−8.1	...	−68.3
2020-11-20 19:15	1.0	267.9	281.1	...	269.3 ± 1.0
2020-11-22 00:14	1.0	267.7	280.9	...	267.3 ± 1.8	−3.3	...	−52.6
2020-11-23 00:30	0.7	267.4	280.7	...	269.5 ± 3.4
2020-11-23 19:44	0.7	267.2	280.5	...	265.7 ± 1.7	−8.2	...	−73.3
2020-11-24 14:45	0.7	266.9	280.3	...	266.6 ± 1.9	−2.0	...	−50.8
2020-11-25 09:59	0.7	266.6	280.1	...	269.5 ± 1.6
2020-11-26 05:15	0.7	266.2	279.9	...	268.1 ± 2.5	13.0	164.2 ± 38.7	...
2020-11-27 00:30	0.7	265.8	279.7	...	267.9 ± 1.8	13.3	165.6 ± 28.8	...
2020-11-27 19:44	0.7	265.3	279.5	...	269.8 ± 1.6
2020-11-28 14:45	0.7	264.8	279.2	...	266.7 ± 2.5	9.5	262.0 ± 80.4	...
2020-11-29 09:59	0.7	264.1	278.9	...	268.3 ± 1.3	25.9	73.9 ± 6.0	...
2020-11-30 05:15	0.7	263.4	278.6	265.3 ± 4.3	263.1 ± 2.4	−1.0	...	−54.9
2020-12-01 00:30	0.7	262.6	278.3	267.6 ± 1.7	263.0 ± 1.4	1.2
2020-12-01 19:44	0.7	261.6	277.9	...	264.0 ± 1.0	7.7	374.8 ± 56.7	...
2020-12-02 14:45	0.7	260.5	277.6	266.9 ± 1.3	263.5 ± 1.3	8.9	325.9 ± 54.7	...
2020-12-03 09:59	0.7	259.2	277.2	...	264.4 ± 1.5	15.3	182.1 ± 21.9	...
2020-12-04 05:15	0.7	257.6	276.8	...	266.0 ± 1.0	25.3	99.8 ± 4.7	...
2020-12-05 00:30	0.7	255.6	276.4	...	265.0 ± 1.4	24.1	111.2 ± 9.1	...
2020-12-05 19:44	0.7	253.1	275.9	268.7 ± 2.3	263.1 ± 1.1	20.9	138.7 ± 9.3	...
2020-12-06 14:45	0.7	249.9	275.5	...	262.9 ± 2.6	23.9	121.1 ± 17.2	...

Notes.

¹ Number of days used to make the median images.

² Position angle of the anti-Sun direction, in degrees, by HORIZONS.

³ Position angle of the negative heliocentric velocity, in degrees, by HORIZONS.

⁴ Position angle of the dust tail and its uncertainty, in degrees.

⁵ Position angle of the plasma tail and its uncertainty, in degrees.

⁶ Aberration angle.

⁷ Inferred solar wind radial velocity from Equation (2). Units of km s^{−1}

The negative values represent w_{nonr} in the same direction as the comet motion and $\epsilon < 0$. Unit km/s.

3.1. Observations of Dust and Plasma Tails

HI-1: a total of 26 HI-1 median images were generated as listed in Table 2. An example median image, from UT 2020 December 5, is shown in the top panel of Figure 4. The STEREO-A images are aligned solar north up (Karl Battams, private communication). Before combination into image medians, we rotated the individual images to equatorial orientation (north up, east left) using the telescope header roll angles. An animation of the median images (Figure 7) shows a bright tail growing longer and brighter as the comet approaches perihelion. The tail position angles are broadly consistent with the antisolar (−*S*) direction. Above the bright long tail, a faint tail branch is seen to have a position angle closer to the negative heliocentric velocity (−*V*) direction.

Both the synchrone and syndyne trajectories have position angles $\theta_{PA} > 270^\circ$, showing that the faint and short upper component in the HI-1 image is the dust tail with characteristic dust particle sizes $\sim 10 \mu\text{m}$. The lower and brighter long tail is the plasma tail.

COR2: 17 median-combined images were generated from the COR2 data, as summarized in Table 3. The left column of Figure 5 displays four selected images, while the middle and right columns show overplotted synchrone and syndyne models. In all images, except for the one from UT 2020

December 10, two tails can be clearly seen, separated from each other. The syndyne dust models fit better to the thick tail profiles compared to the synchrone, suggesting that the dust particles are distributed over a range of sizes, which is consistent with the HI-1 data. Notably, the tail observed around position angle 270° is identified as the dust tail, while the second tail with a variable position angle is attributed to the plasma tail. One remarkable finding from the COR2 image sequence is that while the position angle of the dust tail remains stable near $\theta_{PA} = 270^\circ$, the plasma tail (indicated by orange arrows in Figure 5) exhibits unprecedented and rapid swings around the antisolar direction. This tail swing is prominently captured in the animation shown in Figure 8 and discussed in Section 4.

On December 10, the two tails of the comet appear merged, making it difficult to distinguish one from the other. This merging of the tails lasted from UT December 10 02:00 to December 12 11:15. During this time, the plasma tail is completely invisible at UT December 10 23:29 and December 11 06:45. The position angle of the plasma tail at these times is omitted from Table 3. There are several reasons why the plasma tail may be obscured from observers, while we do recognize that the dust tail is located at $\theta_{PA} \approx 270^\circ$. The small phase angles (see Table 3) and the alignment of the tail with the Sun–comet line may contribute to the plasma tail’s obscurity.

Table 3
Measurements From COR2

Date	Days ^a	α^b	θ_{-S}^c	θ_{-V}^d	θ_{Dust}^e	θ_{Plasma}^f	ϵ^g	w_r^h	w_{nonr}^i
2020-12-08 09:30	0.3	9.14	237.6	274.4	265.0 ± 1.0	182.0 ± 1.5	-13.0	...	-109.7
2020-12-08 18:00	0.3	8.31	233.6	274.2	264.5 ± .71	180.7 ± 7.6	-11.4	...	-104.1
2020-12-09 02:29	0.3	7.52	228.6	274.0	264.8 ± 2.0	150.8 ± 2.6	-14.4	...	-114.8
2020-12-09 11:00	0.3	6.77	222.4	273.8	261.1 ± 1.6	155.6 ± 9.0	-11.6	...	-105.2
2020-12-09 19:15	0.3	6.12	215.0	273.6	260.6 ± 3.9	210.3 ± 5.8	-1.0	...	-68.9
2020-12-10 02:00	0.2	5.68	207.7	273.4	262.2 ± 3.9	235.6 ± 6.3	7.9	465.7 ± 388.5	...
2020-12-10 09:14	0.2	5.30	198.6	273.2	262.0 ± 5.5	247.0 ± 1.8	16.4	215.4 ± 26.7	...
2020-12-10 16:15	0.2	5.08	188.7	273.0	264.5 ± 2.0	233.1 ± 9.4	10.0	367.4 ± 358.0	...
2020-12-10 23:29	0.2	5.01	177.7	272.8	264.7 ± 2.2
2020-12-11 06:45	0.2	5.13	166.8	272.6	259.1 ± 4.5
2020-12-11 14:00	0.2	5.41	156.7	272.4	253.8 ± 1.8	231.9 ± 3.8	14.5	253.8 ± 69.6	...
2020-12-11 21:14	0.2	5.84	147.6	272.2	254.2 ± 10.	226.1 ± 3.3	14.2	260.1 ± 63.6	...
2020-12-12 04:15	0.2	6.37	140.2	272.0	260.0 ± 5.4	219.0 ± 8.9	13.8	268.2 ± 181.6	...
2020-12-12 11:29	0.2	7.01	133.8	271.8	261.0 ± 2.2	208.0 ± 9.7	13.2	284.5 ± 218.9	...
2020-12-12 18:59	0.3	7.75	128.2	271.6	256.8 ± 4.1	156.4 ± 2.1	6.6	573.4 ± 188.7	...
2020-12-13 03:30	0.3	8.64	123.1	271.4	255.8 ± 3.1	159.8 ± 2.6	9.2	413.7 ± 119.0	...
2020-12-13 12:00	0.3	9.59	118.9	271.2	257.8 ± 3.7	157.4 ± 1.6	10.7	353.9 ± 54.3	...

Notes.

^a Number of days used to make the median images.

^b S3 Phase Angle.

^c Position angle of the anti-Sun direction, in degrees.

^d Position angle of the negative velocity, in degrees.

^e Position angle of the dust tail, in degrees.

^f Position angle of the plasma tail, in degrees.

^g Aberration angle.

^h Inferred solar wind radial velocity with measured plasma tail position angle from Equation (2). Unit of km s⁻¹

ⁱ Nonradial solar wind velocity, in units of km s⁻¹. The negative values represent the w_{nonr} in the same direction as the comet motion and $\epsilon < 0$.

The strong background emission from the solar corona also plays a role in masking the plasma tail.

LASCO/C3: the telescope roll angle is not stored in the LASCO FITS headers and therefore, in order to align the C3 images with celestial north, we measured the angle using the positions of known stars in the C3 images. In total, 25 background-suppressed median images (see Table 4) were generated from the LASCO/C3 data. An example is shown in the top panel of Figure 6. The synchro (second panel) and syndyne (third panel) models in Figure 6 reveal the wide large dust tail around a position angle of 270°. At smaller particle sizes of about <30 μm, the syndynes fit to the dust tail better than the synchroes, but the synchroes with longer ejection times (e.g., 100 days) seem to match better to the dust tail. Meanwhile, the plasma tail, indicated by the orange arrow, is well separated from the dust tail.

3.2. Tail Properties

Tail widths: tail width measurements support the identification of the dust and plasma tails. At each position along the tail we measured the FWHM (w) defined as the perpendicular width at half the maximum surface brightness. Figure 9 shows w as a function of distance from the nucleus, with errors estimated by comparing with Gaussian profiles. The nucleus FWHM is about 5 pixels for COR2 and 3 pixels for HI-1 and C3, reflecting the different point-spread functions of the instruments. The HI-1 and C3 cameras provide greater sensitivity to low surface brightness emission against the sky background. We obtain a composite dust tail image with the LASCO/C3 images, and a composite plasma tail image with the HI-1 images. They are embedded in Figure 9. As expected from the dynamics of dust, a linear fit shows that the dust tail is strongly flared, with width

$w = (0.24 \pm 0.02)r + (1.68 \pm 0.24) \times 10^5$ km, where r is the distance from the nucleus in kilometers. By comparison, the width of the plasma tail varies only slightly with increasing distance from the nucleus, consistent with a magnetically confined structure. The fit to the plasma tail yielded $w = (0.01 \pm 0.01)r + (2.42 \pm 0.14) \times 10^5$ km.

Tail lengths: the tails fade progressively to invisibility with increasing distance from the nucleus, allowing only lower limits to the lengths to be placed. A rough estimate of the length was obtained using the DS9 display (Joye & Mandel 2003)⁴ with the *histogram equalization* function on the best tail image. This technique increases the global contrast of images which have a limited range of values. The longest dust tail is found in C3 camera images at 6.5 Mkm. The plasma tail length is given by the HI-1 camera at 10.0 Mkm. The COR2 images are less sensitive to low surface brightness emission and reveal the dust and plasma tails only to ~0.7 Mkm.

Tail position angles: the position angles of the dust and plasma tails (θ_{dust} , θ_{plasma}) are crucial quantities to this study, especially θ_{plasma} . We tried different methods to measure the tail directions, including Gaussian fits to the tail profiles made perpendicular to their axes. In the end, the tail position angles were determined manually by fitting a straight line to data points along the axes with uncertainties determined from multiple measurements. The position angles of the tails were measured counterclockwise from celestial north (see the images shown as examples in Figures 4, 5, and 6). Figure 10 shows the position angles as functions of time, where the three panels present observations from wide-field camera HI-1 (top), narrow-field camera COR2 (middle), and LASCO/C3

⁴ <http://ds9.si.edu/doc/ref/how.html>

Table 4
Measurements From LASCO/C3

Date	Days ^a	θ_{-S} ^b	θ_{-V} ^c	θ_{Dust} ^d	θ_{Plasma} ^e	ε ^f	w_r ^g
2020-12-18 23:45	0.4	292.9	252.5	263.1 ± 1.3	273.5 ± 2.6	39.7	91.9 ± 6.9
2020-12-19 10:30	0.4	295.3	252.4	262.9 ± 2.3	275.9 ± 2.5	30.8	120.4 ± 10.3
2020-12-19 21:14	0.4	297.9	252.2	263.0 ± 1.4	274.0 ± 1.7	41.2	88.5 ± 4.1
2020-12-20 08:15	0.4	300.8	252.0	265.2 ± 3.4	274.6 ± 2.8	40.0	91.6 ± 7.2
2020-12-20 18:59	0.4	303.9	251.9	263.3 ± 2.6	275.8 ± 4.1	37.3	98.7 ± 11.6
2020-12-21 05:45	0.4	307.1	251.7	266.4 ± 2.2	274.0 ± 2.3	46.8	76.9 ± 4.4
2020-12-21 16:30	0.4	310.6	251.6	267.2 ± 2.3	274.6 ± 4.8	45.6	79.2 ± 9.4
2020-12-22 03:14	0.4	314.2	251.4	267.1 ± 2.1	281.4 ± 3.5	28.2	129.0 ± 15.7
2020-12-22 14:15	0.4	318.0	251.2	267.5 ± 1.1	289.3 ± 4.7	18.8	187.2 ± 43.7
2020-12-23 00:59	0.4	321.9	251.1	266.3 ± 1.9	283.3 ± 4.0	28.4	126.5 ± 16.9
2020-12-23 11:45	0.4	325.8	250.9	268.9 ± 3.0	281.0 ± 4.5	34.0	106.0 ± 13.5
2020-12-23 22:30	0.4	329.7	250.8	266.6 ± 2.9	282.5 ± 6.1	32.9	109.0 ± 1.9
2020-12-24 09:14	0.4	333.6	250.6	267.1 ± 1.5	286.5 ± 5.6	28.7	123.1 ± 22.4
2020-12-24 20:15	0.4	337.5	250.5	268.3 ± 3.4	299.0 ± 2.8	18.4	182.5 ± 25.6
2020-12-25 06:59	0.4	341.1	250.3	267.9 ± 2.7	293.0 ± 6.3	24.7	138.8 ± 32.0
2020-12-25 17:45	0.4	344.6	250.2	268.4 ± .98	296.1 ± 7.9	23.6	143.8 ± 43.6
2020-12-26 04:30	0.4	348.0	250.0	267.8 ± 2.8	292.8 ± 5.8	27.7	123.4 ± 23.5
2020-12-26 15:14	0.4	351.1	249.9	268.5 ± 2.6	322.2 ± 5.2	11.8	262.1 ± 105.4
2020-12-27 02:15	0.4	354.1	249.8	269.6 ± 1.6	315.3 ± 3.3	16.3	194.7 ± 35.4
2020-12-27 12:59	0.4	356.8	249.6	269.5 ± 3.0	323.9 ± 3.1	13.8	223.8 ± 45.4
2020-12-27 23:45	0.4	359.3	249.5	269.3 ± 3.7	331.7 ± 6.9	11.8	254.5 ± 135.3
2020-12-28 10:30	0.4	361.6	249.4	269.7 ± 3.7	337.8 ± 2.2	10.6	278.0 ± 52.9
2020-12-28 21:14	0.4	363.7	249.2	272.1 ± 5.1	335.6 ± 5.0	12.6	234.1 ± 84.0
2020-12-29 08:15	0.4	365.7	249.1	271.5 ± 3.9	343.7 ± 1.7	10.5	271.8 ± 41.7
2020-12-29 18:59	0.4	367.5	249.0	272.3 ± 1.5	343.0 ± 1.8	11.9	240.5 ± 33.2

Notes.

^a Number of days used to make the median images.

^b Position angle of the anti-Sun direction, in degrees.

^c Position angle of the negative velocity, in degrees.

^d Position angle of the dust tail, in degrees.

^e Position angle of the plasma tail, in degrees.

^f Aberration angle.

^g Inferred solar wind radial velocity with measured plasma tail position angle from Equation (2). Units of km s^{-1}

(bottom). Blue and orange circles distinguish the position angles of the dust and plasma tails, respectively. The solid blue and red curves respectively represent the position angles of $-V$ and $-S$ viewed from each telescope. The measured position angles and their uncertainties are also listed in Tables 2, 3, and 4).

4. Discussion

The discussion will be focused on the plasma tail. The position angles of the tail are used to infer the solar wind speed and other conditions.

4.1. Determination of the Plasma Tail Aberration Angle

The comet aberration angle is measured in the comet orbital plane (Figure 11). At the comet position, C, a number of quantities are plotted with respect to the Sun: the cometary velocity V (and the antimotion velocity $-V$) and anti-Sun direction $-S$. The comet and its plasma tail are represented by a brown tail-like image. It extends to the opposite direction of V forming an aberration angle ε with respect to the $-S$ direction (Sun–comet line). The tail intercepts with another anti-Sun direction $-S_p$, marking the Sun–comet line at an earlier time. As the comet moves along its orbit, its progression can be measured with the comet’s true anomaly, which is the angle in the orbital plane from the perihelion direction to the comet, measured positively in the direction of motion. At the time of

observation (t), the comet’s true anomaly is ν . But the comet’s plasma tail tilts backward opposite to the motion direction, corresponding to the true anomaly ν_p at an earlier time (t_p). As a result, $t - t_p > 0$ and $\Delta\nu = \nu - \nu_p > 0$. Under assumption that the cometary tails lie in the orbital plane, we have a triangle of the Sun–comet–intercept point of the comet tail with the Sun–comet line in the $-S_p$ direction. In this triangle, r is the heliocentric distance of the comet and L is the length of the comet tail. The comet’s aberration angle is simply calculated as $\varepsilon = \Delta\nu + \eta$. We note that this relation is independent of the tail length, L , regardless how η and $\Delta\nu$ change in quantity. Taking $\eta \rightarrow 0$, we can reasonably put $\varepsilon \sim \Delta\nu$.

To determine $\Delta\nu$, we use the relation between the true anomaly (ν) and the position angle of the anti-Sun direction ($-S$) projected to the observer’s sky plane (θ_{-S}). The relation $\nu(t) = f(\theta_{-S}(t))$ is established by the quantities “Tru_Anom” and “PsAng” in the JPL Horizons’ “Observer Table.” The observed position angle of the plasma tail (θ_{plasma}) often differs from the $-S$ direction (θ_{-S}) (see Figure 10), which results in a different true anomaly from a different time $\nu_p = f(\theta_{\text{plasma}})$ on the orbital plane. Figure 12 demonstrates the comet’s true anomaly ν (light blue circles) at the observing times and the true anomaly ν_p (gray circles) corresponding to the observed tail position angles at different times. Both ν and ν_p fall along the $\nu(t) = f(\theta_{-S}(t))$ function curve (black solid curve). On the top panel for HI-1, five gray data points are off the function curve. The aberration angles cannot be resolved for these data

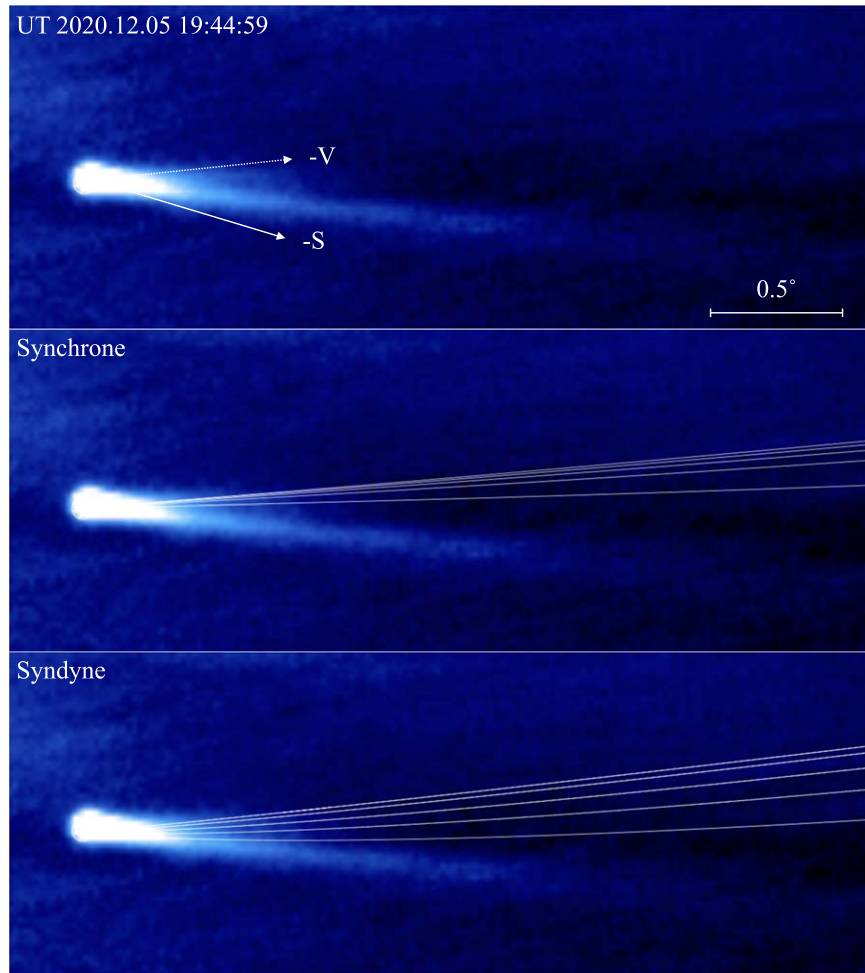


Figure 4. An example image taken with the HI-1 wide-field camera. Top: the median image from UT 2020 December 05. The anti-Sun ($-S$) and antiorbital ($-V$) directions are indicated by solid and dashed arrows, respectively. The bright long tail is the plasma tail. The faint tail above the plasma tail is the dust tail. The middle and bottom panels are the modeled synchrones and syndynes overlapping the image. Synchrones were computed for ejection times of 20, 40, 60, 80, and 100 days prior to the date of observation (curves from bottom to top, in the figure). Syndynes were computed for $\beta = 1, 0.3, 0.1, 0.03,$ and 0.01 (curves from bottom to top), corresponding to nominal particle radii of 1, 3, 10, 30, and 100 μm , respectively. Celestial north is up, east is to the left. The region shown is $3.2^\circ \times 1.2^\circ$ (160×60 pixels).

points. This underscores the limitation of the technique. As a result, these five data points are left with ε listed in Table 2. They also appear above the dotted horizontal line on the top panel (HI-1) of Figure 10.

Figure 13 shows the aberration angle (ε) derived from the observed position angle of the plasma tail (θ_{plasma}) as a function of time. The errors in the observed position angles (see Figure 10) are adapted for the errors of the observed aberration angles, $\Delta\varepsilon$. The aberration angles also are found in the column ε in Tables 2, 3, and 4. For those data points with $\varepsilon \sim \Delta\nu = \nu - \nu_p > 0$, the indication is that the tail tilts away from the comet’s motion; for those data points where $\varepsilon < 0$, the tail is tilted forward in the same direction as the orbital motion (V).

4.2. Solar Wind Velocity Inferred from the Plasma Tail Position Angles

From Equation (1), the solar wind radial velocity can be inferred to be

$$w_r = \frac{v_t}{\tan \varepsilon} + v_r. \quad (2)$$

The errors are estimated from

$$\Delta w_r = \left| -\frac{v_t}{\sin^2 \varepsilon} \right| \Delta \varepsilon, \quad (3)$$

where $\Delta\varepsilon$ is in units of radians. The units for w_r , v_t , and Δw_r are km s^{-1} .

The cometary radial velocity v_r and the absolute velocity v are known quantities provided by JPL Horizons. The tangential component is $v_t = \pm \sqrt{v^2 - v_r^2}$, where $v_t > 0$ as it points at the comet motion direction. The inferred solar wind velocity and error bars are shown in Figure 14 as functions of heliocentric distance (top), longitude (middle), and latitude (bottom). They are found in the “ w_r ” columns of Tables 2, 3, and 4. The data points with $\varepsilon < 0$ are not presented with the values of w_r because such aberrations are probably caused by other phenomena rather than the radial solar wind, as we will discuss in the following sections. Some solar wind velocity data points have very large uncertainties. These data points are often coincident with aberration angles $\varepsilon \lesssim 2^\circ$. This is especially evident for the HI-1 observations (see Table 2).

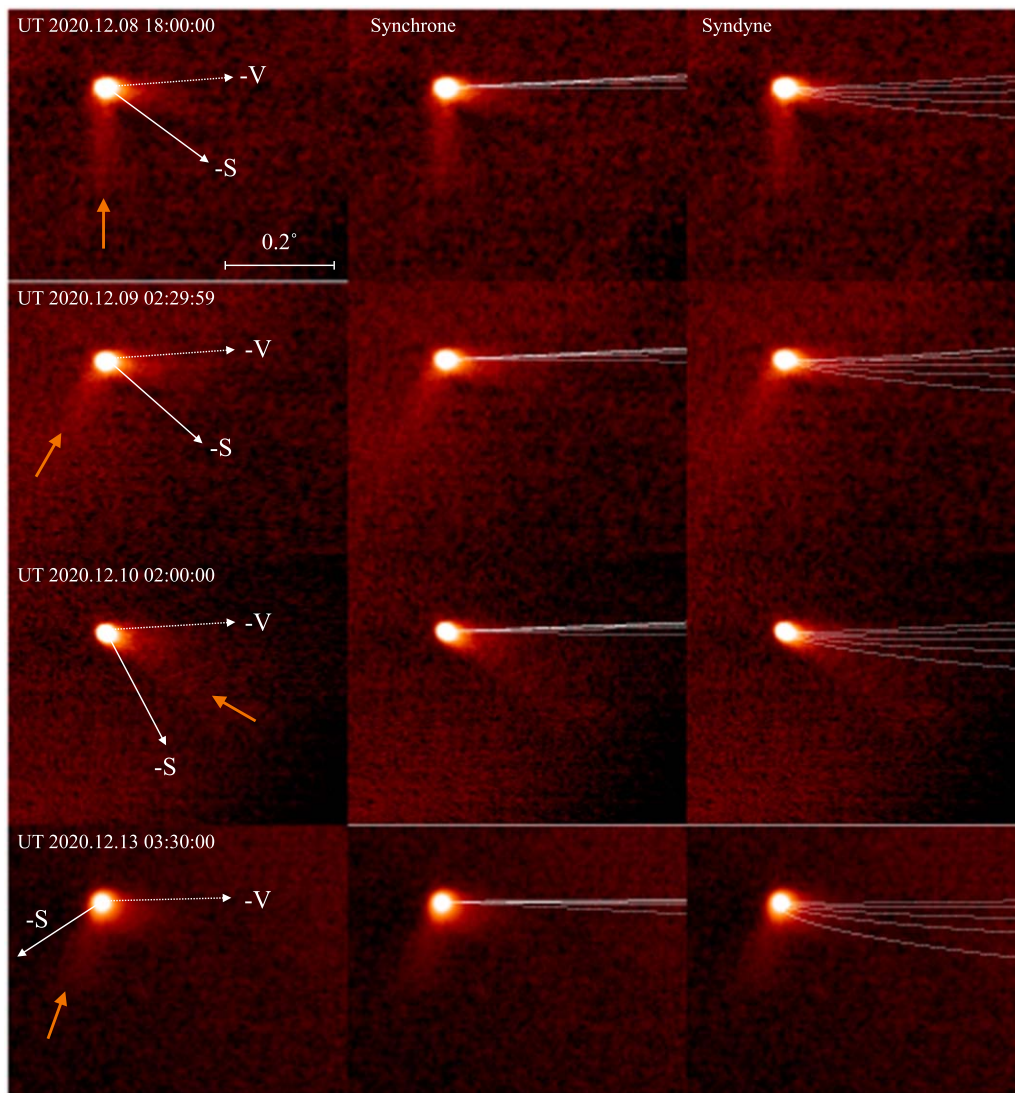


Figure 5. Left column: examples of median COR2 images showing the rapidly changing position angle of the plasma tail (indicated by orange arrows). The anti-Sun ($-S$) and anti-orbital velocity ($-V$) directions are indicated by solid and dotted arrows, respectively. Middle and right columns: the superimposed loci of synchrones and syndynes computed with same parameters as in Figure 4. Celestial north is up and east to the left. The region shown is $\sim 0.6^\circ \times 0.5^\circ$ (150×120 pixels).

Figure 14 consists of two sets of plots, with the left side showing the solar wind radial velocity as a function of heliocentric distance, longitude, and latitude as S3 moves inbound toward the Sun. The right side, on the other hand, shows the same quantities but as the comet moves outbound away from the Sun. S3 appears to be in the slow solar wind velocity domain during the observations, with wind speeds approximately doubling as the comet travels inbound compared to its outbound journey.

To verify the solar wind environment around S3, we compare the solar wind measurements with large-scale, physics-based space weather prediction models known as Wang–Sheeley–Arge (WSA)–Enlil solar wind predictions. These models are generated at the Space Weather Prediction Center (SWPC),⁵ which provides advance warning of solar wind structures and Earth-directed CMEs.

We downloaded the models generated by SWPC for the period from 2020 mid-November to the end of December. We

⁵ <https://www.swpc.noaa.gov/productswsa-enlil-solar-wind-prediction>

examine models of the solar wind velocity structures in the ecliptic plane, looking down from above solar north. The positions of Earth, STEREO-A, and STEREO-B are also given in the simulations, allowing for a comparison between the model results and the actual observations made by STEREO-A and SoHO. The models predict solar wind velocities $< 550 \text{ km s}^{-1}$ during the HI-1 observations, $< 400 \text{ km s}^{-1}$ during the COR2 observations, and $< 300 \text{ km s}^{-1}$ during the C3 observations. The models have a minimum velocity of 200 km s^{-1} , while the observed solar wind velocities are often $< 200 \text{ km s}^{-1}$ around S3 on the comet’s journey both inbound and outbound (Figure 14). One possibility is that the solar wind mass loading due to pick up of cometary ions may decelerate the solar wind (Omidi & Winske 1987). The evidence is that the solar wind velocities are $< 100 \text{ km s}^{-1}$ as S3 nears perihelion ($< 0.455 \text{ au}$) with the exception of observations taken in the COR2 visibility window.

4.3. Plasma Tail Influenced by a Nonradial Solar Wind Flow

On the top panel of Figure 13, some data points have $\varepsilon < 0$, meaning that the tails tilt forward in the cometary motion

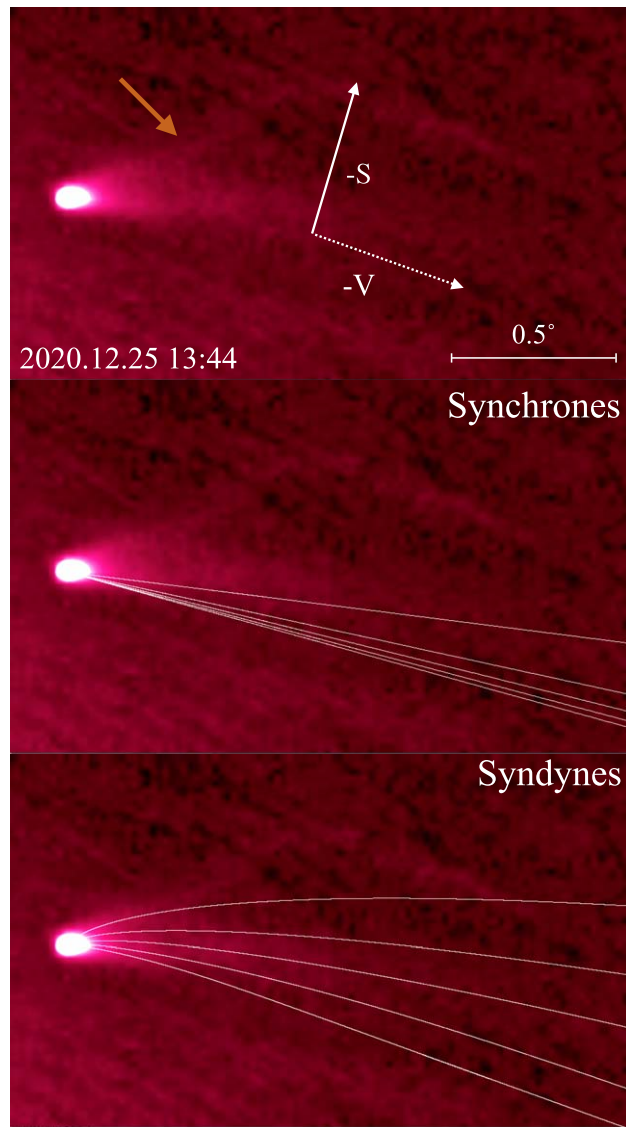


Figure 6. Top: an example of a median image of LASCO/C3. $-V$ (dotted arrow) and $-S$ (solid arrow) represent the antimotion and anti-Sun directions, respectively, at the location of the comet. The plasma tail is indicated by an orange arrow. Middle and bottom panels: the computed synchrone and syndyne models superimposed on the comet image to simulate the dust tails. The solid white curves are the modeled synchrones and syndynes calculated with the same parameters as those in Figure 4. North is up, east is to the left, and the region shown is $\sim 1.9 \times 1.6$ (120×100 pixels).

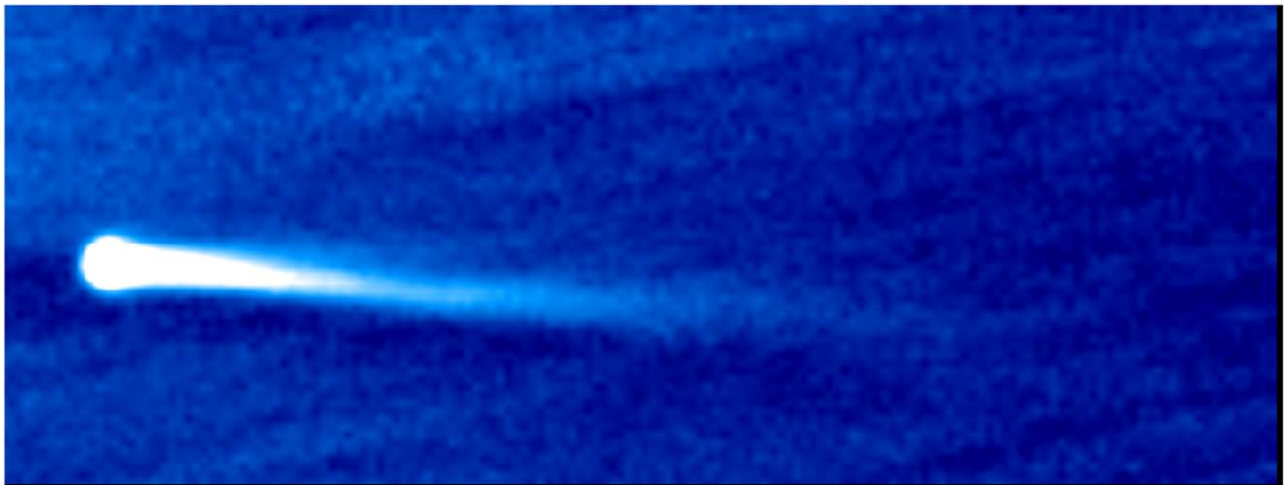


Figure 7. S3 in the HI-1 camera. This is one frame from the animated series shown in the electronic edition. The bright tail is plasma. The faint, approximately horizontal structure above the plasma tail is dust. Image size is 3.2×1.2 (160×60 pixels). (An animation of this figure is available.)

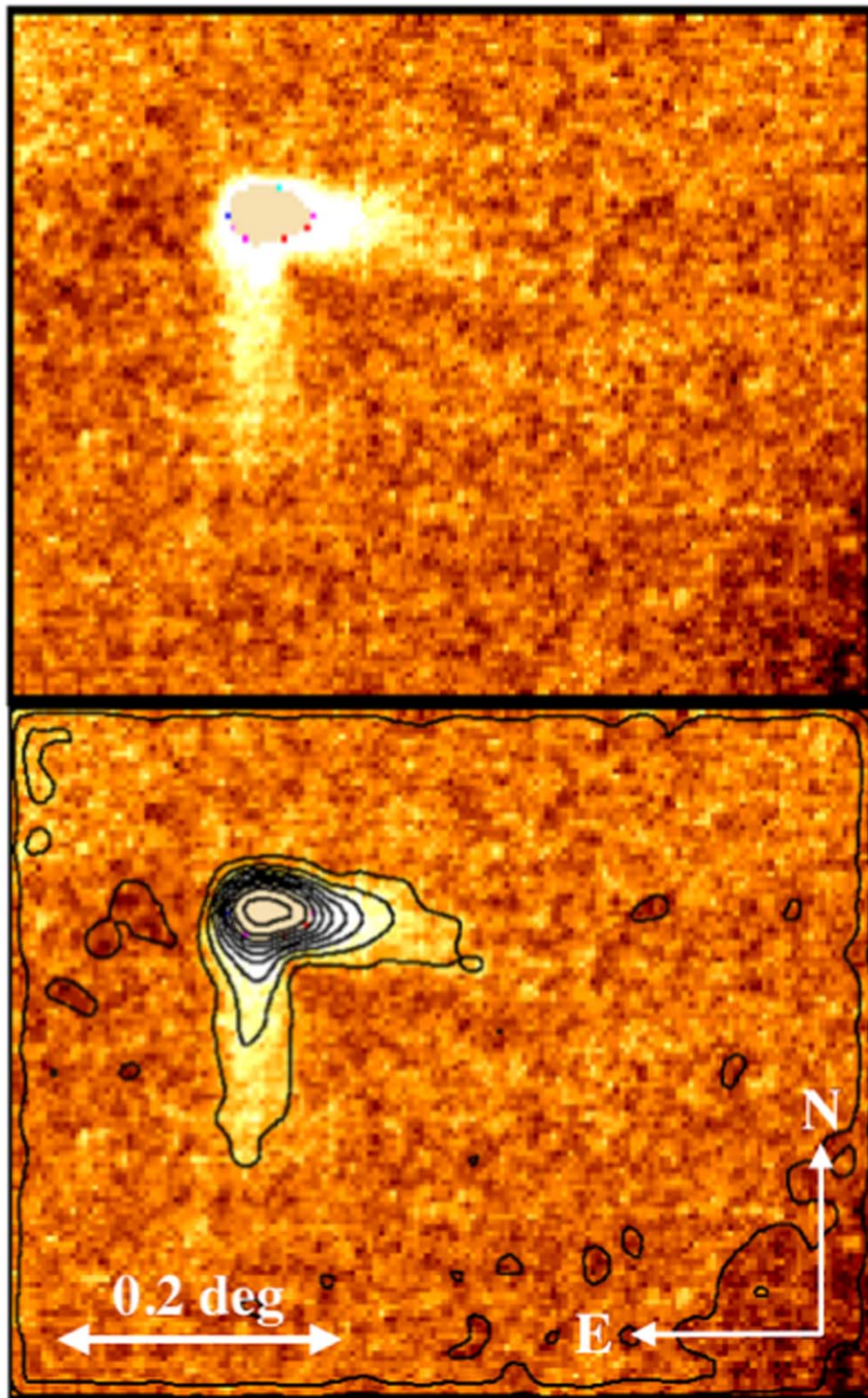


Figure 8. COR2 camera image shown in raw (upper) and contoured (lower) formats. The plasma tail points to the south and the dust tail to the west in this image. An animation including this image is available in the electronic edition. Image size is 0.6×0.5 (150×120 pixels).

(An animation of this figure is available.)

direction opposite to the nonradial flows carried by solar rotation (Weber & Davis 1967). This implies the presence of an azimuthal solar wind flow against an Archimedes spiral, which is about a few kilometers per second according to the analytical models of Tasnim & Cairns (2016). Equation (1) can be slightly modified by replacing v_t with $v_t + w_{nonr}$. Then the

nonradial velocity component can be estimated with ε as

$$w_{nonr} = \tan \varepsilon (w_r - v_r) - v_t, \quad (4)$$

where v_t and v_r are the cometary tangential and radial components of the orbital velocity, respectively, w_r is the solar wind radial velocity, and ε is simply the angle of the plasma tail

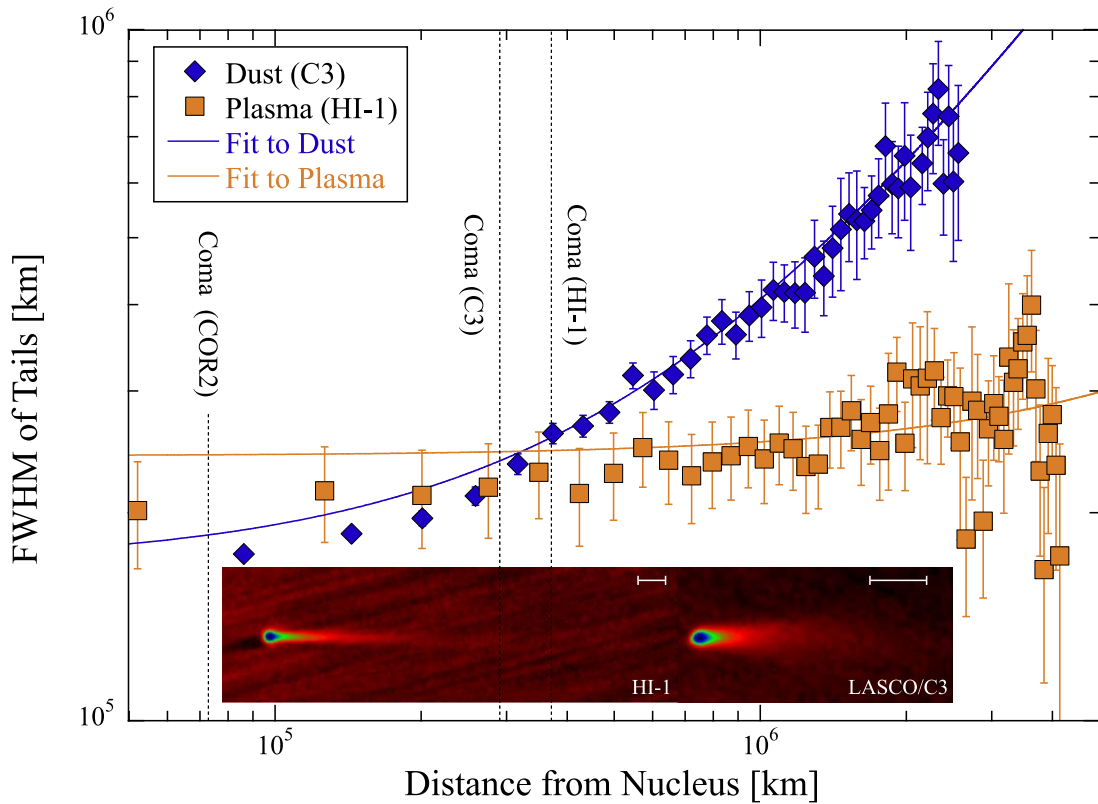


Figure 9. FWHM of the comet tails as a function of distance from the nucleus. The error bars are 3σ uncertainties of the tail width computed from the Gaussian fits. The coma positions are marked with vertical dotted lines for each camera. The embedded images are composites of the HI-1 and LASCO/C3 images from which the widths are measured (dust widths are from LASCO/C3 and plasma widths are from HI-1). Scale bars on the images are 1 Mkm at the comet.

with respect to the solar radial direction in negative values. The azimuthal component of the solar wind due to an Archimedes spiral is omitted in this estimation. Therefore, Equation (4) gives a lower limit to the nonradial solar wind component in the cometary motion direction. Given an average $w_r = 183.6 \text{ km s}^{-1}$ during the HI-1 observations, we obtain an average nonradial velocity $\sim -66.8 \text{ km s}^{-1}$ in the same period. The negative value represents the nonradial velocity direction against the corotating direction. The individual inferred w_{nonr} values corresponding to each data point are listed in the last column of Table 2.

Several causes can result in nonradial solar wind flows. A survey of nonradial flows during nearly 5 yr of observation reveals that the average nonradial flow speed is $\sim 30 \text{ km s}^{-1}$. Furthermore, about half of the nonradial flow events are associated with interplanetary coronal mass ejections (ICMEs) with average speeds exceeding 100 km s^{-1} (Owens & Cargill 2004). The cause of a nonradial flow by a CME is the diversion of flow in the sheath region behind an ICME shock front due to compression of the shock wave (Gosling et al. 1987). Another possible cause of nonradial flow are corotating interaction regions (CIRs), which can play a role in deflecting the fast and slow solar wind flows azimuthally in opposite directions (Gosling & Pizzo 1999). In the absence of detectable ICMEs, we investigate whether CIRs are responsible for the observed nonradial flows during the time period under study (DOY 318.6 to 329.6, as shown in the top panel of Figure 14). Enlil models are examined for clues regarding the presence of corotating streams. The models show that the

corotating streams swept through the path of S3 with velocities ranging from 200 to 550 km s^{-1} . However, without careful examination of the comet’s path overlapping with the corotating regions, it is challenging to determine with certainty whether the nonradial flows are caused by CIRs, although this remains a possibility.

4.4. Plasma Tail and ICME

The most noteworthy feature in our data is a rapid change in the plasma tail position angles occurring as soon as the comet enters the COR2 field of view. The plasma tail position angles swing like a pendulum by an amount that is very large compared to the measurement uncertainties (see the first five data points in the middle panel of Figure 10). The tail position angle began at $\theta_{\text{plasma}} \sim 180^\circ$ in the first two data points, decreased to $\sim 150^\circ$, and then abruptly swung near the antisolar direction ($\sim 210^\circ$). Despite the dramatic change in position angles in the observer frame, the tail angles with respect to the Sun–comet line show a more modest variation. The average $-\varepsilon \sim -12.7 \pm 3.5$ in the comet’s orbital plane (see the middle panel of Figure 13) among the first four data points (period ~ 25.5 hr). The tail angle then swings back over the next ~ 8.5 hr to near the Sun–comet line (0°) as it is shown with the fifth data point in the figure, and thereafter to $\sim +15^\circ$. The abnormal tail orientation lasted at least ~ 34 hr.

We searched for evidence to support the conjecture that the plasma tail of S3 might have been deflected by a CME. While there are no in situ observations to confirm an ICME interaction with S3, we do indeed find a halo CME which occurred on UT

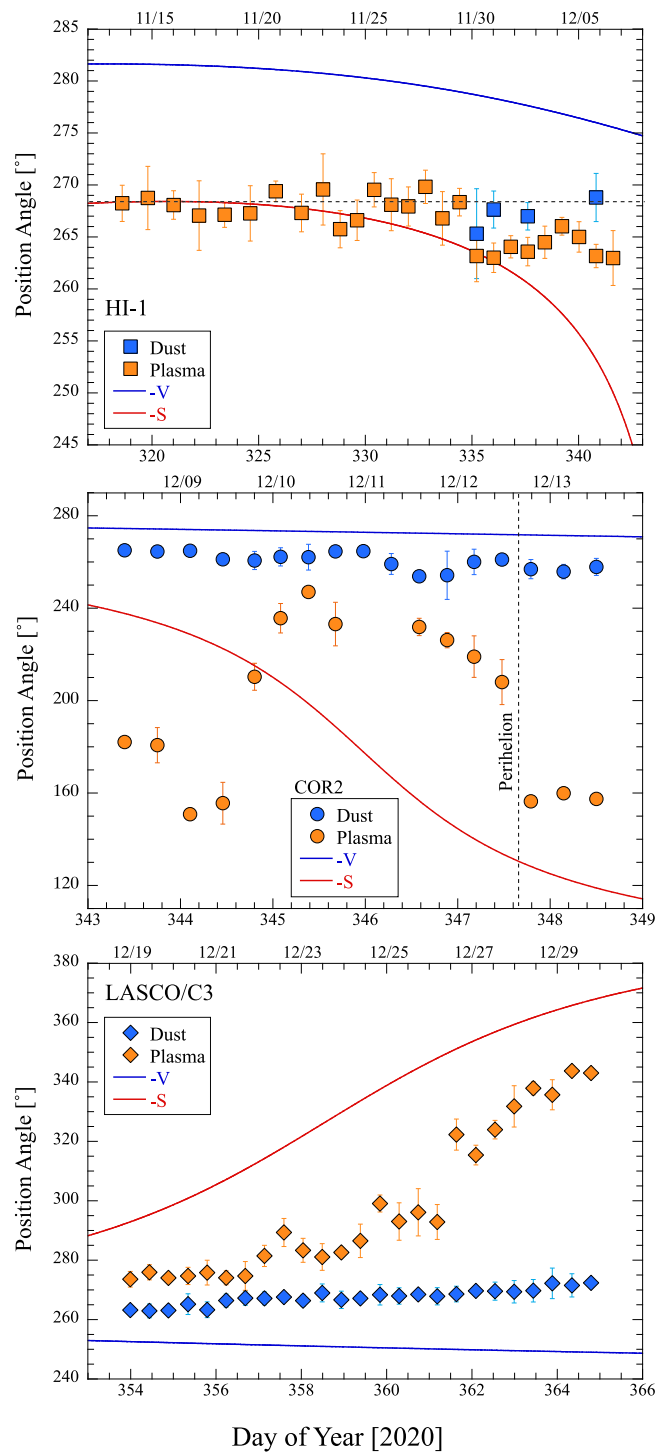


Figure 10. Time dependence of the position angle of the dust (blue) and plasma (orange) tails from HI-1 (top), COR2 (middle), and C3 (bottom). Position angle uncertainties on some points are comparable to the size of the symbols used to plot the data. Red and blue solid curves are the anti-Sun ($-S$) and anti-orbital-motion ($-V$) directions, respectively. The time of perihelion is marked with a vertical dotted line on the COR2 (middle) panel. The data points are presented in Tables 2, 3, and 4. Note that five orange data points are above the horizontal dotted line in the top panel. The comet aberration angles cannot be resolved with these data points using the current technique. The calendar dates are shown on the top horizontal axis.

2020 December 7.68 in the NASA SoHO LASCO CME catalog.⁶ Using the Helioviewer (Müller et al. 2017)⁷ tool, we identify the likely source of the CME as NOAA Active Region 12786. This active region had rotated to the far side of the Sun from

STEREO-A at the time of the comet observation (see Figure 2), meaning that the halo CME traveled directly toward the comet, which was also on the far side of the Sun from STEREO-A. Given the 0.418 au heliocentric distance of S3 and an estimated speed of 1407 km s^{-1} ,⁸ the travel time for the CME front to

⁶ https://cdaw.gsfc.nasa.gov/CME_list

⁷ <https://www.helioviewer.org>

⁸ https://cdaw.gsfc.nasa.gov/CME_list/UNIVERSAL_ver1/2020_12/univ2020_12.html

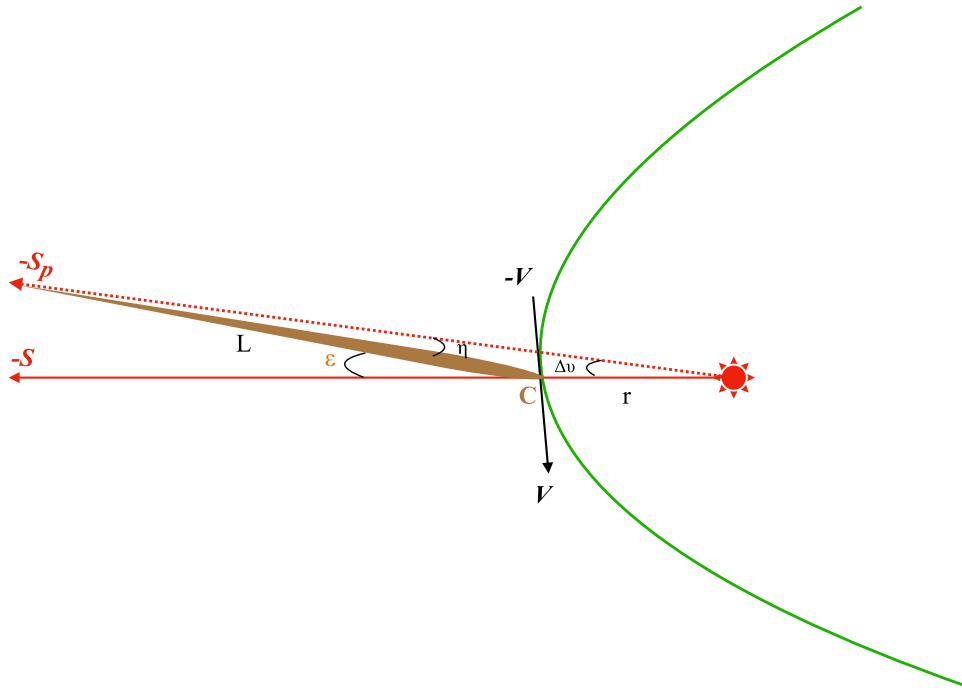


Figure 11. The comet’s orbit (green arc) viewed from above, where r is the comet’s heliocentric distance, V is the comet’s orbital velocity, $-S$ is the antisolar direction, $-S_p$ is the antisolar direction corresponding to the comet’s aberration, ϵ is the aberration angle, $\Delta\nu = \nu - \nu_p$ (where ν is the true anomaly at the observing time and ν_p is the true anomaly at the time associated with the observed tail position angle), L is the plasma tail length, and η is the angle between $-S_p$ and the plasma tail axis. The relation $\epsilon = \eta + \Delta\nu$ is independent of tail length. Taking $\eta \rightarrow 0$, $\epsilon \sim \Delta\nu$.

reach the comet is ~ 12.4 hr, corresponding to arrival on UT December 8.2 (DOY 343.2). This arrival time approximately matches the tail wagging motion detected in the COR2 data (Figure 10). Furthermore, the 34 hr timescale of the tail disturbance is comparable to the ~ 30 hr average ICME crossing time (Wu & Lepping 2011). In the last column of Table 3, we listed the nonradial wind velocity estimated with $\epsilon < 0$ using Equation (4). The average nonradial velocity is $> 100 \text{ km s}^{-1}$, quite consistent with the nonradial velocities caused by CMEs found in the survey by Owens & Cargill (2004). While it is possible that the CME and the tail disturbance are only coincidentally related, we note that comparable CMEs are comparatively rare; only two such events occurred in the entire month of December. In this interpretation, the absence of tail wagging in the earlier HI-1 and later C3 observations occurs simply because no other ICME impacts S3 during those times. After passing an ICME, the tail angle should naturally return close to the solar wind radial direction, as observed in Figure 10 in the middle panel. We conclude that the plasma tail swing in COR2 is plausibly attributed to interaction with an ICME.

5. Summary

We present near-perihelion observations of long-period comet S3 from the STEREO-A and SoHO spacecraft. The STEREO-A camera HI-1 and the coronagraph COR2 captured the comet from ~ 0.836 au to perihelion at 0.398 au. About 4.3 days later, the comet was imaged by the LASCO/C3 coronagraph over the outbound heliocentric distance range ~ 0.427 – 0.658 au. The comet moved from heliocentric latitude -20° to 20° and longitude 119° to 285° during our observations. In order to understand the comet plasma tail motions in the observer’s sky plane, a simple technique is

developed to obtain the comet aberration angle (ϵ) from the observed position angle of the plasma tail. We summarize the observations and conclusions below.

1. We detected a large and transient excursion in the position angle of the plasma tail on UT 2020 December 8, from 180° to 150° then back to 210° , lasting about 34 hr. The excursion cannot be caused by changes in the speed of the solar wind. However, the excursion is coincident with the passage of an ICME. We find that NOAA AR 12786 launched a halo CME with a direction and time consistent with the observed deflection of the comet tail.
2. We detected long-duration ($\gtrsim 11$ days) wagging of the plasma tail about the Sun–comet line caused by nonradial flows. The Enlil solar wind models show that the corotating streams swept through the path of the comet with velocities ranging from 200 to 550 km s^{-1} . However, careful examination of the comet’s path overlapping with the corotating regions is needed to determine with certainty whether the nonradial flows are caused by CIRs, although this remains a possibility.
3. Wind speeds inferred from the position angles range from ~ 73.9 to $\sim 573.5 \text{ km s}^{-1}$, showing that S3 was in the slow solar wind region. This is confirmed by the Enlil models during the observation period. The average (median) solar wind radial velocity is 205.5 (182.3) km s^{-1} as the comet moves in space. The velocities show a very rough increase with decreasing heliocentric latitude in the STEREO-A observations. On the other hand, they tend to increase slightly with increasing heliocentric latitude in LASCO/C3.
4. The average (median) plasma tail aberration angle is $20^\circ.3$ ($16^\circ.3$) with minimum and maximum values $\epsilon = 1^\circ.2$ and $\epsilon = 46^\circ.8$, respectively.

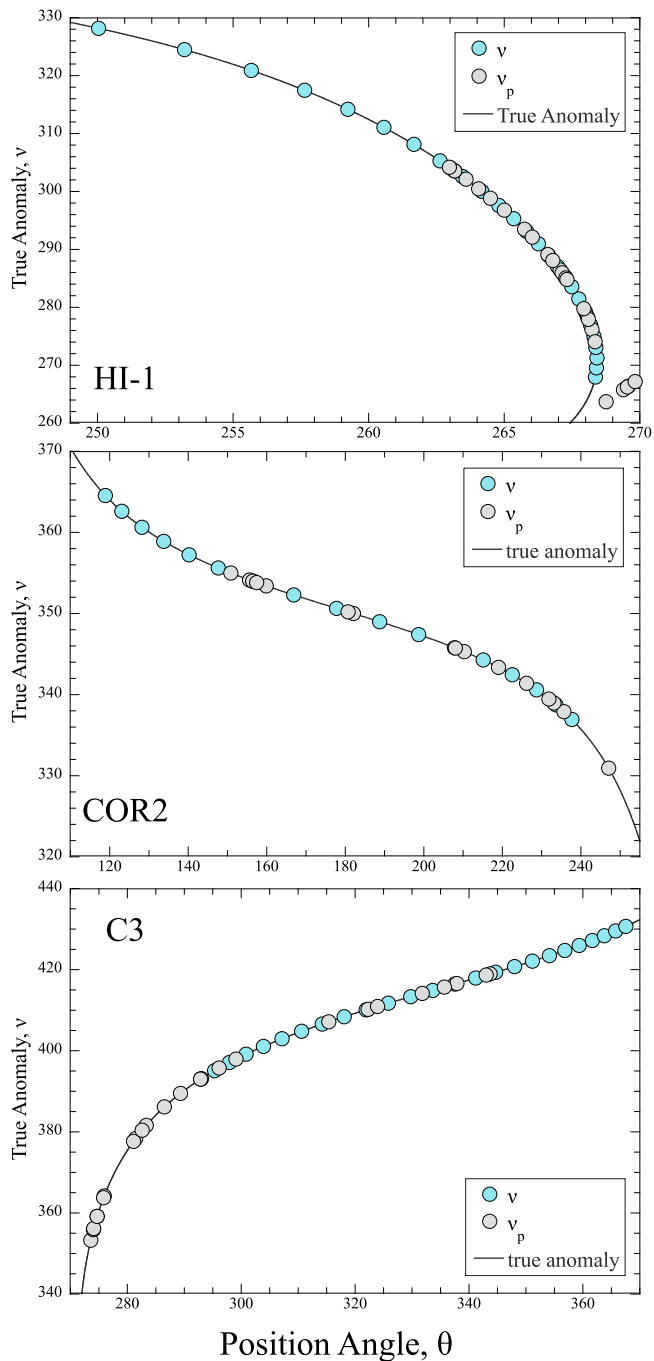


Figure 12. The comet’s true anomaly (ν) as function of antisolar position angle (θ). Functions are plotted as solid black curves provided by JPL Horizons in all three panels. Light blue circles represent the comet’s true anomaly (ν) at the time of observation. Gray circles represent the comet’s true anomaly (ν_p) inferred from the tail position angles (θ_{plasma}). The three panels correspond to the HI-1, COR2, and C3 instruments. Note the five gray data points are not on the black curve on the top panel for HI-1. The true anomaly cannot be solved for these data points.

5. The technique to obtain the comet’s aberration relies on accurate measurements of the position angle of the plasma tail in the equatorial frame. Therefore, knowledge of the telescope roll angle between spacecraft image frames and the celestial coordinates is crucial. The technique is valid under the assumption that the comet tails lie in the orbital plane. The inferred solar wind radial velocity becomes unreliable when $\varepsilon < 2^\circ$.

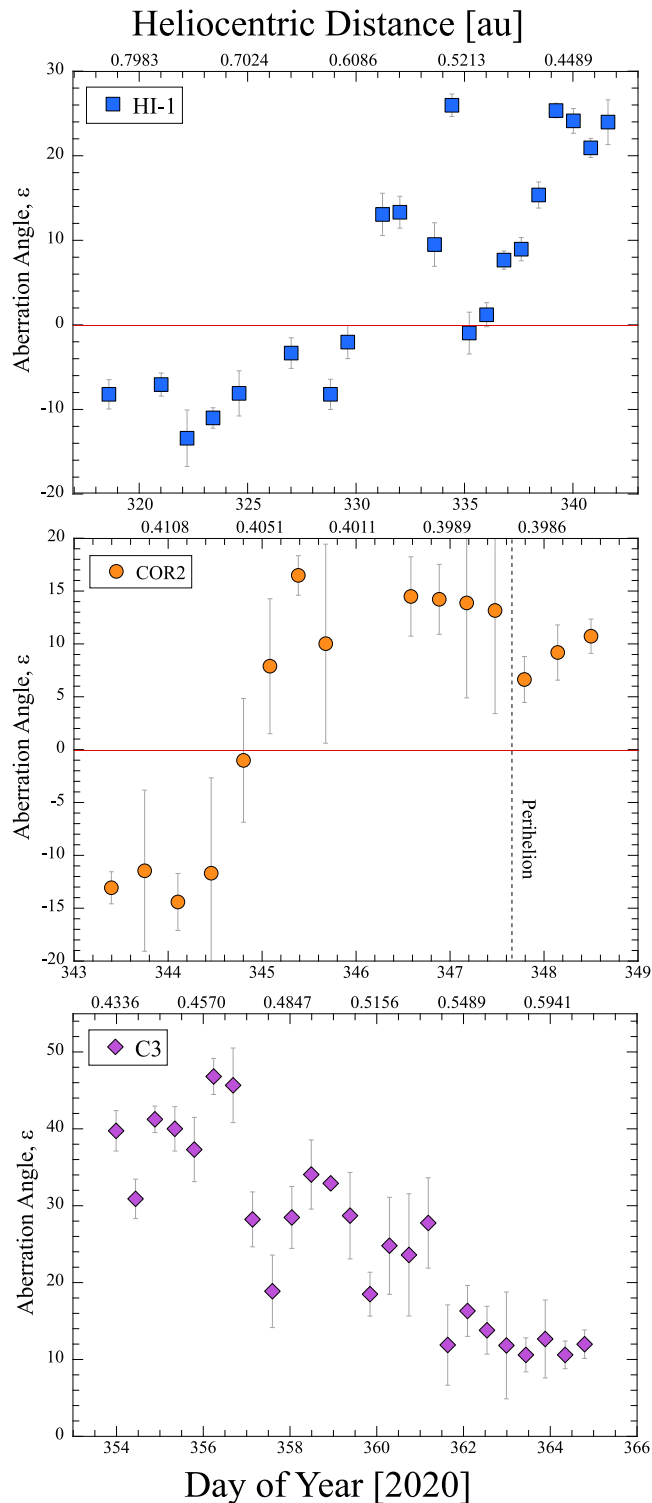


Figure 13. The comet plasma tail aberration angles as a function of time (bottom horizontal axis) and heliocentric distance (top horizontal axis) in the comet’s orbital plane. The three panels show the measurements from the three instruments: HI-1 (top), COR2 (middle), and C3 (bottom). Red horizontal lines show the Sun–comet line, $\varepsilon = 0^\circ$.

6. The dust tail is spatially distinguished from the plasma tail in the COR2 and LASCO/C3 cameras, but only marginally resolved in the HI-1 data. Comparison with synchro and syndyne dust models indicates that the dust tail is dominated by particles with $\beta \sim 0.1$, corresponding to characteristic sizes of order $10 \mu\text{m}$.

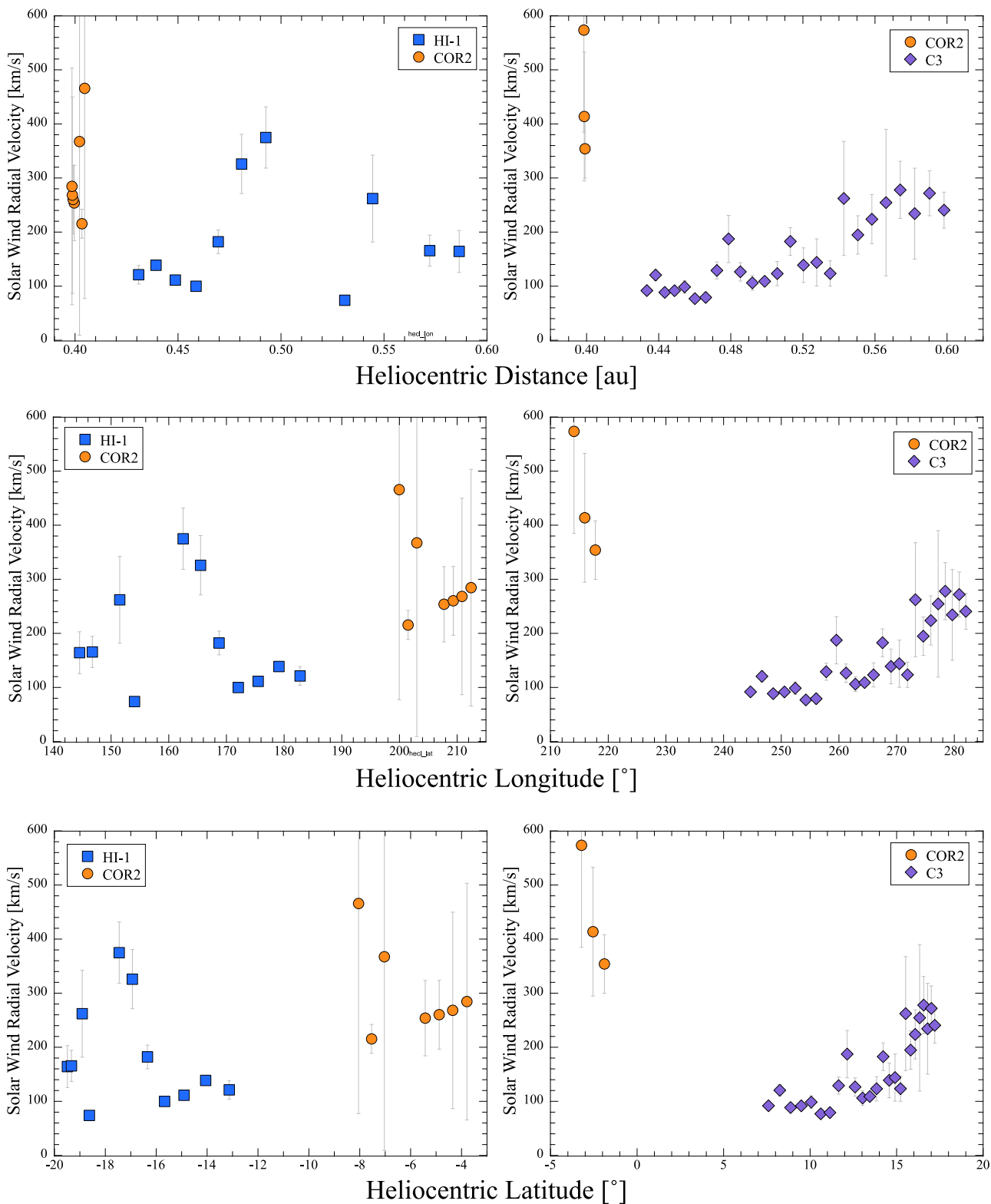




Figure 14. Inferred solar wind radial velocity as functions of heliocentric distance (top), longitude (middle), and latitude (bottom). The three plots on the left present the solar wind velocities as S3 moves inbound; those on the right present the solar wind as S3 moves outbound. The symbols distinguish measurements made with HI-1 (blue squares), COR2 (orange circles), and LASCOCO/C3 (purple diamonds).

Acknowledgments

We thank Drs. Yingdong Jia, John Raymond, Pedro Lacerda, Masateru Ishiguro, and Bin Yang for reading the manuscript and providing comments. We would like to express our gratitude to the anonymous referee whose critical comments urged us to re-

examine the observational data. We are grateful to Dr. William Thompson for prompt help with world coordinate system questions, and general data reduction. Dr. Bernhard Fleck was also very kind to help with our inquiries. Dr. Karl Battams advised us regarding LASCOCO/C3 image rotations.

ORCID iDs

Jing Li  <https://orcid.org/0000-0002-0982-7309>
 Yoonyoung Kim  <https://orcid.org/0000-0002-4676-2196>

References

- Alfvén, H. 1957, *Tell*, **9**, 92
 Belton, M. J. S., & Brandt, J. C. 1966, *ApJS*, **13**, 125
 Biermann, L. 1951, *ZAp*, **29**, 274
 Bohren, C. F., & Huffman, D. R. 1983, *Absorption and Scattering of Light by Small Particles* (New York: Wiley), 1983
 Brandt, J. C. 1968, *ARA&A*, **6**, 267
 Brueckner, G. E., Howard, R. A., Koomen, M. J., et al. 1995, *SoPh*, **162**, 357
 Bryans, P., & Pesnell, W. D. 2012, *ApJ*, **760**, 18
 Buffington, A., Bisi, M. M., Clover, J. M., et al. 2008, *ApJ*, **677**, 798
 Cheng, L., Wang, Y., & Li, X. 2022, *ApJ*, **928**, 121
 Cheng, L., Zhang, Q., Wang, Y., et al. 2020, *ApJ*, **897**, 87
 Clover, J. M., Jackson, B. V., Buffington, A., et al. 2010, *ApJ*, **713**, 394
 Combi, M. R., Mäkinen, T., Bertaux, J.-L., et al. 2023, *Icar*, **398**, 115543
 Cremonese, G., Boehnhardt, H., Crovisier, J., et al. 1997, *ApJL*, **490**, L199
 Cremonese, G., Huebner, W. F., Rauer, H., et al. 2002, *AdSpR*, **29**, 1187
 Domingo, V., Fleck, B., & Poland, A. I. 1995, *SoPh*, **162**, 1
 Downs, C., Linker, J. A., Mikić, Z., et al. 2013, *Sci*, **340**, 1196
 Eyles, C. J., Harrison, R. A., Davis, C. J., et al. 2009, *SoPh*, **254**, 387
 Finson, M. J., & Probst, R. F. 1968, *ApJ*, **154**, 327
 Freeland, S. L., & Handy, B. N. 1998, *SoPh*, **182**, 497
 Gosling, J. T., & Pizzo, V. J. 1999, *SSRv*, **89**, 21
 Gosling, J. T., Thomsen, M. F., Bame, S. J., et al. 1987, *JGR*, **92**, 12399
 Howard, R. A., Moses, J. D., Vourlidas, A., et al. 2008, *SSRv*, **136**, 67
 Hui, M.-T. 2023, *AJ*, **165**, 94
 Hundhausen, A. J. 1968, *SSRv*, **8**, 690
 Ip, W.-H., & Mendis, D. A. 1976, *Icar*, **29**, 147
 Jackson, B. V., Buffington, A., Clover, J. M., et al. 2013, *Solar Wind*, **13**, 1539, 364
 Jewitt, D., & Li, J. 2010, *AJ*, **140**, 1519
 Jia, Y. D., Russell, C. T., Jian, L. K., et al. 2009, *ApJL*, **696**, L56
 Jones, G. H., Knight, M. M., Battams, K., et al. 2018, *SSRv*, **214**, 20
 Joye, W. A., & Mandel, E. 2003, *adass XII*, **295**, 489
 Kaiser, M. L., Kucera, T. A., Davila, J. M., et al. 2008, *SSRv*, **136**, 5
 Kohl, J. L., Esser, R., Gardner, L. D., et al. 1995, *SoPh*, **162**, 313
 Müller, D., Nicula, B., Felix, S., et al. 2017, *A&A*, **606**, A10
 Niedner, M. B., & Brandt, J. C. 1978, *ApJ*, **223**, 655
 Niedner, M. B., & Brandt, J. C. 1979, *ApJ*, **234**, 723
 Niedner, M. B., Rothe, E. D., & Brandt, J. C. 1978, *ApJ*, **221**, 1014
 Nisticò, G., Zimbardo, G., Perri, S., et al. 2022, *ApJ*, **938**, 20
 Omid, N., & Winske, D. 1987, *JGR*, **92**, 13409
 Owens, M., & Cargill, P. 2004, *AnGeo*, **22**, 4397
 Oyama, K. I., & Hirao, K. 1985, *AdSpR*, **5**, 65
 Parker, E. N. 1958, *ApJ*, **128**, 664
 Povich, M. S., Raymond, J. C., Jones, G. H., et al. 2003, *Sci*, **302**, 1949
 Ragot, B. R., & Kahler, S. W. 2003, *ApJ*, **594**, 1049
 Ramanjooloo, Y., & Jones, G. H. 2022, *JGRA*, **127**, e29799
 Raymond, J. C., Downs, C., Knight, M. M., et al. 2018, *ApJ*, **858**, 19
 Raymond, J. C., Giordano, S., Mancuso, S., et al. 2022, *ApJ*, **926**, 93
 Tasnim, S., & Cairns, I. H. 2016, *JGRA*, **121**, 4966
 Thompson, W. T., & Wei, K. 2010, *SoPh*, **261**, 215
 Uzzo, M., Raymond, J. C., Biesecker, D., et al. 2001, *ApJ*, **558**, 403
 Voelzke, M. R. 2005, *EM&P*, **97**, 399
 Vourlidas, A., Davis, C. J., Eyles, C. J., et al. 2007, *ApJL*, **668**, L79
 Weber, E. J., & Davis, L. 1967, *ApJ*, **148**, 217
 Wegmann, R. 2000, *A&A*, **358**, 759
 Wu, C.-C., & Lepping, R. P. 2011, *SoPh*, **269**, 141
 Zhang, Q., Battams, K., Ye, Q., et al. 2023, *PSJ*, **4**, 70